Title

Redox-Active Supramolecular Polymer Binders for Lithium–Sulfur Batteries That Adapt Their Transport Properties in Operando

Journal

Chemistry of Materials, 28(20)

ISSN

0897-4756

Authors

Frischmann, Peter D
Hwa, Yoon
Cairns, Elton J
et al.

Publication Date

2016-10-25

DOI

10.1021/acs.chemmater.6b03013

Peer reviewed

Article

Redox-Active Supramolecular Polymer Binders for Lithium–Sulfur Batteries that Adapt their Transport Properties In Operando

Peter D. Frischmann, Yoon Hwa, Elton J. Cairns, and Brett A. Helms

Chem. Mater., **Just Accepted Manuscript** • DOI: 10.1021/acs.chemmater.6b03013 • Publication Date (Web): 25 Sep 2016

Redox-Active Supramolecular Polymer Binders for Lithium–Sulfur Batteries that Adapt their Transport Properties In Operando

Peter D. Frischmann[§,‡], Yoon Hwa[∫,‡], Elton J. Cairns[∫,Σ,*] Brett A. Helms[§,†,*]

§ The Joint Center for Energy Storage Research, Lawrence Berkeley National Laboratory, One Cyclotron Rd., Berkeley, California, 94720, USA

∫ Energy Technologies Area, Lawrence Berkeley National Laboratory, One Cyclotron Rd., Berkeley, California, 94720, USA

Σ Department of Chemical and Biomolecular Engineering, University of California, Berkeley, California, 94720, USA

† The Molecular Foundry, Lawrence Berkeley National Laboratory, One Cyclotron Rd., Berkeley, California, 94720, USA

ABSTRACT: π-Stacked perylene bisimide (PBI) molecules are implemented here as highly networked, redox-active supramolecular polymer binders in sulfur cathodes for lightweight and energy-dense Li–S batteries. We show that the in operando reduction and lithiation of these PBI binders sustainably reduces Li–S cell impedance relative to non-redox active conventional polymer binders. This lower impedance enables high-rate cycling in Li–S cells with excellent durability, a critical step toward unlocking the full potential of Li–S batteries for electric vehicles and aviation.

INTRODUCTION

Breakthroughs in battery electrodes that enable energy-dense, high-power, and low-cost energy storage are necessary to catalyze a societal shift from fossil fuels to a carbon-neutral future powered by renewable energy. Of the forward-looking battery chemistries, lithium–sulfur (Li–S) cells offer certain advantages over more established Li-ion chemistries with respect to the high theoretical specific capacity of the sulfur cathode (1675 mAh g^{-1} *vs.* 272 mAh g^{-1} for a $LiCoO_2$ cathode), the low cost of sulfur (<$200 ton^{-1}), the low environmental impact of sulfur, and the improved safety of the cell.[1–6] Nevertheless, persistent challenges associated with the sulfur cathode must be overcome for Li–S cells to become practical. For example, while sulfur cathodes have been engineered extensively for high energy density and durability,[7–23] design rules are still lacking for high power while also attaining high specific energy.

Here we show that transport bottlenecks for ions and electrons in composite sulfur cathodes, presently limiting high-power applications, can be relieved when the conventional polymer binder is supplanted with a custom-purposed supramolecular polymer binder that is also a redox-mediator for the sulfur cell chemistry (Figure 1). These supramolecular redox mediators consist of π-stacked perylene bisimide (PBI) molecules, which are reduced electrochemically *in operando* during the first discharge at potentials below 2.5 V *vs.* Li/Li^+. We show that upon activation, the cell impedance is dramatically reduced and commensurate with stable cycling at both moderate and high current densities. We also note unexpected synergies between these redox-mediating supramolecular binders and conventional polymer binders when both are present in the sulfur cathode. These synergies manifest as a powerful new means to direct the evolution of cell impedance to a state that is lower than cells assembled with either of the binders on their own; furthermore, we show that this state of the cell is sustainable throughout high-rate cycling. Our work highlights the multi-faceted role played by these underappreciated components in the sulfur cathode, and where new concepts in adaptive materials can be applied to solve challenges in charge transport.

Binders for composite sulfur cathodes should aid in electrode processing and drying onto aluminum current collectors, electrolyte wetting during cell assembly, ion transport, and mechanical integrity upon cycling to accommodate the volume changes associated with S_8–Li_2S interconversion.[24,25] Polyvinylidene difluoride (PVDF) is the most prevalent binder used today, although recent reports have suggested that PVDF can block the pores of mesostructured conductive carbons, which negatively impacts the available surface area for Li_2S deposition.[26]

Alternative binders—including gelatin,[27] polyvinylpyrrolidone (PVP),[28] PVP blends with Nafion,[29] PAMAM dendrimers,[30] polycationic β-cyclodextrins,[31] polyacrylic acid,[32] polyethylene oxide,[33] and carboxymethylcellulose:styrenebutadiene-rubber (CMC:SBR)[34,35]—have therefore focused on addressing one or more of these binder attributes as a means to improve cathode performance. Some of the most successful binders have been shown to mitigate the migration of soluble polysulfides from the cathode into the electrolyte, which otherwise would lead to stranded sulfur in the cell or instabilities in the lithium anode.[36] None have been reported that directly participate in the redox chemistry of sulfur or otherwise serve to enhance ion transport as needed for high-rate applications. Nonetheless, we hypothesize that these attributes are critical to the further advancement of the sulfur cathode. Our perspective is that these functions can now be

conferred to new binder materials based on supramolecular redox mediators. Supramolecular redox mediators offer both self-healing properties needed to accommodate the volume changes in the sulfur cathode on cycling and adaptive charge transport upon activation. Their role as such remains distinctive from electronically conductive polymers used to confine sulfur.[37,38]

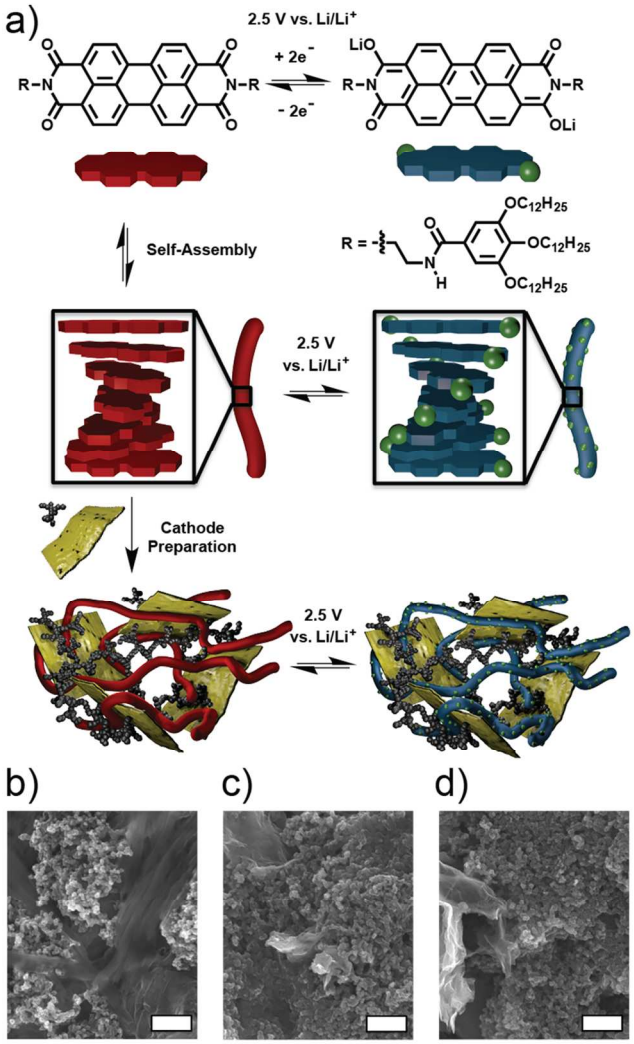

Figure 1. a) Overview of perylene bisimide (PBI) redox chemistry, self-assembly of PBI into supramolecular polymers through π-stacking, cathode preparation with Ketjenblack (KB) and sulfur on graphene oxide (S–GO), and *in operando* redox activation of the PBI binder in a functioning cathode. The neutral PBI binder (red) is activated to a dianionic state (Li_2-PBI, blue) upon reduction at 2.5 V *vs.* Li/Li^+. SEM images of: b) the PBI cathode showing bundles of supramolecular polymer wires, macrophase-separated from both KB and S–GO in the formulation; c) the PVDF cathode, showing well-blended composites with respect to PVDF, KB, and S–GO; and d) the PBI/PVDF cathode, showing well-blended composites with PBI/PVDF, KB, and S–GO. Scale bars represent 400 nm.

EXPERIMETNAL SECTION

Instrumentation. Contact angle measurements were performed using a Krüss EasyDrop. Scanning electron micrographs were taken using the in-lens detector of a Zeiss Gemini Ultra-55 outfitted with energy-dispersive X-ray spectroscopy (EDS, JEOL JSM-7500F) for elemental mapping. Thermo gravimetric analysis (TGA – TA Instruments, SDT-Q600) was used to determine the weight content of the S in the CTAB-modified S–GO nanocomposite with a heating rate of 10 $^oC\ min^{-1}$ under N_2 atmosphere. Cell testing was performed on an Arbin BT2000 cycler. Electrochemical impedance spectroscopy was conducted with a BioLogic VMP3 potentiostat. Raman was performed on a Horiba Jobin Yvon LabRAM ARAMIS automated scanning confocal Raman microscope.

Materials. PBI was synthesized according to a literature procedure.[39] Lithium nitrate (Alfa Aesar, $LiNO_3$, Anhydrous, 99.999 %), lithium metal (FMC), bis(trifluoromethanesulfonyl)imide lithium salt (Aldrich, LiTFSI), PVDF (Kureha, KF-1100), *N*-methyl-*N*-butylpyrrolidinium bis(trifluoromethane sulfonyl)imide (Coorstek), *N*-methyl-2-pyrrolidone (Alfa Aesar, 99+%), dioxolane (Sigma Aldrich, 99.8 %), dimethoxyethane (Sigma Aldrich, 99.9 %), Sodium sulfide (Alfa Aesar, Na_2S, anhydrous), sulfur (Alfa Aesar, S, ~ 325 mesh, 99.5 %), Graphene oxide (ACS Material), cetyltrimethyl ammonium bromide (Sigma Aldrich, CTAB, $CH_3(CH_2)_{15}N(Br)(CH_3)_3$), formic acid (Aqua Solutions). Ketjen Black (AkzoNobel EC-600JD).

Preparation of the CTAB-modified S−GO nanocomposite. The CTAB-modified S−GO nanocomposite was prepared *via* a published method.[13] Briefly, 0.58 g of sodium sulfide powder was dissolved in 25 mL ultrapure water to form a Na_2S solution. 0.72 g elemental sulfur powder was added to the Na_2S solution and stirred with a magnetic stirrer at 60 ˚C until the solution became transparent orange color (a sodium polysulfide (Na_2S_x) solution). 18 mL of single layer graphene oxide dispersion (GO, 10 mg mL^{-1}) in water was diluted to form a GO suspension (180 mg of GO in 180 mL of ultrapure water). 2.5 mM of cetyltrimethyl ammonium bromide (CTAB, $CH_3(CH_2)_{15}N(Br)(CH_3)_3$) were added to the GO suspension and stirred for 2 h with a magnetic stirrer. Then, the prepared Na_2S_x solution was added to the GO-CTAB composite solution and stirred overnight. The as-prepared Na_2S_x–GO-CTAB composite solution was slowly added to 100 mL of 2.0 M formic acid (HCOOH) and stirred for 2 h to precipitate elemental S onto the GO. Finally, the CTAB-modified S–GO nano-composite was filtered and washed with acetone and ultrapure water several times to remove salts and impurities. The obtained powder sample was dried at 50 ˚C in a vacuum oven overnight. The dried powder sample was ground using mortar and pestle and heat-treated in a tube furnace at 155 ˚C for 12 h under Ar atmosphere.

Contact Angle Measurement. Composite cathodes identical to those tested in coin cells were prepared with PBI, PVDF, and PBI/PVDF. The EasyDrop instrument was placed in a glove bag and purged with N_2 for 1 h to prevent water uptake by the hygroscopic electrolyte from altering the measurement. PVDF and PBI/PVDF electrodes wet immediately by electrolyte and would not sustain a drop for contact angle measurement, whereas the PBI electrode showed a contact angle of 56˚ as is depicted in Figure S7.

Li–S Cell Electrochemical Measurements. The sulfur cathodes were prepared by mixing the S–GO nanocomposite, carbon black (black) with a binder (either the PBI, PVDF, or PBI/PVDF composite binder 1:1 by weight) at a weight ratio of 8:1:1 in *N*-methyl-2-pyrrolidone (NMP) solvent to form a slurry using magnetic stirrer. All Slurries were heated to 100

°C while stirring to completely dissolve the PBI binder into NMP and uniformly casted *via* a doctor blade on aluminum foil. The cathode was first dried at room temperature for 24 h, and then dried in a vacuum oven at 50 °C for 24 h to fully eliminate any solvent residue. Composite films cast in this manner were devoid of any gross structural aberrations and no delamination was observed with any of the binder constructs used, suggesting excellent adhesion to Al in all cases. The average sulfur loading of the cathodes was 0.8–1.0 mg cm^{-2}. 1 M Lithium Bis(Trifluoromethanesulfonyl)Imide (LiTFSI) in *N*-methyl-*N*-butylpyrrolidinium bis(trifluoromethane sulfonyl)imide ($PYR_{14}TFSI$)/dioxolane (DOL)/Dimethoxyethane (DME) (2:1:1, *v/v/v*) containing 1 wt% $LiNO_3$ was prepared for the electrolyte and 70 µL were added to each cell. CR2325-type coin cells were fabricated with a lithium metal foil as counter/reference electrode and a porous polypropylene separator (2400, Celgard) in a glove box filled with Ar gas. Cyclic voltammetry for the prepared cells was conducted using a potentiostat with a voltage range of 1.5 to 2.8 V for 5 cycles at a constant scan rate of 0.1 mV s^{-1}. The prepared cells were discharged and charged at 0.1 C rate using a procedure that consisted of galvanostatic discharge and charge pulses, each 45 min long, followed by 1 h of relaxation time, with open circuit status until the cell voltage reaches 1.5 V and the electrochemical impedance was measured from 10 mHz to 1 MHz using a potentiostat at the end of every relaxation step during discharge and charge. Galvanostatic cycling test of the coin cells was performed using a battery cycler between 1.5 and 2.8 V at 1.0 C and 0.5 C for discharge and charge, respectively. Rate capability tests were also performed at various discharge C rates from 0.1 C to 3.0 C and then back to 0.1 C. All manipulations involving lithium metal were performed in an Ar-filled glove box with water and O_2 content below 2.0 ppm.

Raman Spectroscopy. Roughly 5 mg samples were pressed into pellets of 200–400 µm thickness. PBI containing samples were also examined but the fluorescence from PBI was too high. The PVDF + LiTFSI sample was prepared by soaking a pellet of PVDF in 1:1 dioxolane:DME with 1.0 M LiTFSI for 1 week, followed by drying under high vacuum. This soaking process was performed to allow for mixing of the $TFSI^-$ with the PVDF as it might occur in an actual cathode.

RESULTS AND DISCUSSION

Redox mediators for sulfur cathode reactions—which nominally occur at 2.5 V and 2.1 V *vs.* Li/Li^+—have only been recently reported.[40–43] Those consisting of polycyclic aromatic hydrocarbons, and in particular perylene bisimide[44,45] (PBI) and benzo[*ghi*]perylene imide (BPI), as reported by us, are amenable to supramolecular polymerization via π-stacking. Whereas our previous accounts focused on the action of soluble redox mediators in Li–S cells, our focus here is instead on their action in the solid state as a binder. Ideally, the redox-mediating binder should be easily cast with the other components of the composite sulfur cathode, yet not re-dissolve into the liquid electrolyte once the cathode is assembled into a Li–S cell.

We were ultimately successful in sequestering PBI-based redox-mediators as self-assembled networks of nanowires, tens of microns in length, in a composite sulfur cathode by re-designing imide substituents as inspired by Würthner and co-workers.[39] The networked PBI binder architecture—readily apparent in the solid state (Figure S1) as well as in the cathode composite (Figure 1b and S4)—remained intact upon electrolyte infiltration (i.e., the imide substituents did not allow the PBI network to dissolve into the Li–S battery electrolyte). The redox-active PBI core of our supramolecular binder exhibits a fully reversible two-electron reduction around 2.5 V *vs.* Li/Li^+ (Figure 1a & Figure S7), which aids in charge transfer to and from polysulfides in Li–S cells.[39] Additionally, their manifestation as a percolated network suggests highly structured regions within the cathode (Figure 1b) that are both lithiated and solvated. We anticipate that this architecture helps localize Li^+ ions near active material as needed for high interfacial ion flux. We were also interested in mixed-binder approaches consisting of PBI/PVDF blends in that each component features complementary coordination for Li^+ (which is oxophillic, favoring PBI microdomains) and $TFSI^-$ (which is fluorophillic, favoring PVDF microdomains), respectively. To those points, alkali metal coordination to PBI^{2-} is well-studied;[40,44,45] we also carried out Raman spectroscopy—where $TFSI^-$ features a high-intensity Raman band near 740 cm^{-1}—to highlight the explicit coordination of $TFSI^-$ to PVDF in the solid-state (Figure S8).[46–48] This unusual complementarity between the ionic species in LiTFSI and the PBI and PDVF microdomains could enable higher mobility for ionic charge carriers in the composite sulfur cathode.

To demonstrate the performance-enhancing features of PBI supramolecular polymers in Li–S cells, we interfaced them with a cetyltrimethyl ammonium bromide (CTAB)-modified sulfur-graphene oxide (S−GO) nanocomposite[13] (80% S *w/w*, Figure S2 and S3) as the active material in the cathode. Three distinctive cathodes were prepared using CTAB modified S-GO, Ketjenblack (KB) as conductive carbon additive, and various binders in a 8:1:1 weight ratio; binders included pure PBI nanowire networks, pure PVDF, and a 1:1 blend of PBI and PVDF (PBI/PVDF). Slurries of these components in *N*-methyl-2-pyrrolidinone (NMP) were coated onto aluminum foil current collectors by doctor-blade coating and yielded cathodes with a sulfur content of 64% (*w/w*) after drying. Scanning electron micrographs of each composite sulfur cathode indicated macroscopic film homogeneity, however, differences in the PBI network architecture were observed for cathodes prepared using PBI when compared to those prepared using PBI/PVDF blends (Figure 1b-d and S4–6). More specifically, the introduction of PVDF to the PBI cathode appears to disrupt the bundling of PBI nanowires in the solid state, indicative of high interfacial area between the two materials as well as higher interfacial area with S−GO and KB. Reduced bundling of PBI nanowires in the PBI/PVDF cathode also improved the bulk electrolyte wettability relative to the PBI cathode (Figure S9).

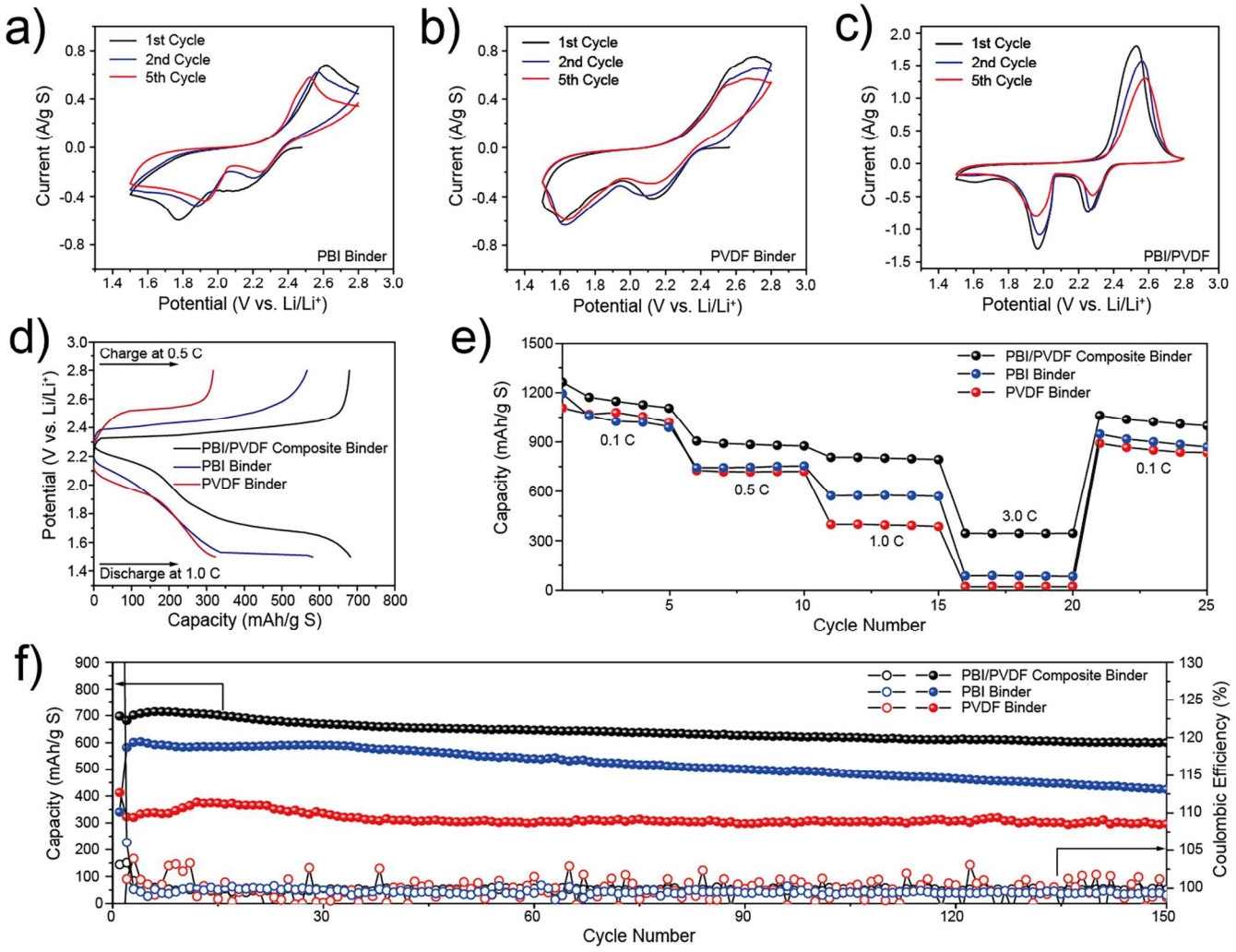

Figure 2. Cyclic voltammograms and electrochemical performances of (a) PBI, (b) PVDF and (c) PBI/PVDF composite binder cathodes. Cyclic voltammograms of (a) PBI, (b) PVDF and (c) PBI/PVDF composite binder cathodes at a scan rate of 0.1 mV s^{-1}. (d) Voltage profiles of PBI, PVDF, and PBI/PVDF composite binder cathodes at the second cycle. (e) Rate capability of of PBI, PVDF and PBI/PVDF, composite binder cathodes. The charge C-rate was fixed at 0.1 C. (f) Cycling performances and Coulombic efficiency of PBI, PVDF, and PBI/PVDF composite binder cathodes at 1.0 C discharge.

The electrochemical behavior of sulfur cathodes prepared with PBI, PVDF, or PBI/PVDF binders was investigated using cyclic voltammetry (CV) over the potential range 1.5−2.8 V *vs.* Li/Li^+ and at a scan rate of 0.1 mV s^{-1} (Figure 2a-c). All three cathodes showed two reduction peaks and one oxidation peak during the discharge and charge processes, respectively; however, the CV peak characteristics of the three cathodes were significantly different. After the first cycle, two reduction peaks and an anodic peak of the PBI cathode were located at 2.3, 1.9 V and 2.6 V, respectively (Figure 2a), whereas those of the PVDF cathode were located at 2.1, 1.6 V and 2.7 V (Figure 2b), indicating that larger peak shifts occurred in the CV of the PVDF cathode than that of the PBI cathode due to the larger overpotential of the PVDF cathode. Moreover, the redox peaks in the CV for the PVDF cathode were broader and less distinguishable than those of the PBI cathode. The incomplete anodic peak of the PVDF cathode is especially noteworthy and reflects the slow reaction kinetics of the PVDF cathode. In contrast, the PBI/PVDF composite binder cathode exhibited the lowest overpotential with sharp peaks located at 2.3 V and 2.0 V for the cathodic peaks and at 2.55 V for the anodic peak, indicating that the highest reaction rate for the sulfur cathode is facilitated by the PBI/PVDF binder blend.

To evaluate the impact of these distinctive electrochemical behaviors on cell performance, PBI, PVDF, and PBI/PVDF composite binder cathodes were galvanostatically cycled at 1.0 and 0.5 C (1.0 C = 1672 mA g^{-1} S) for the discharge and charge processes, respectively (Figure 2d). During the discharge process at 1.0 C, the PBI cathode showed two major discharge plateaus with a capacity of 582 mAh g^{-1} S, whereas the PVDF cathode showed no obvious second plateau associated with the formation of Li_2S, which caused a low sulfur utilization of only 323 mAh g^{-1} S. On the other hand, the PBI/PVDF composite cathode delivered the highest discharge specific capacity of 700 mAh g^{-1} S with the lowest discharge and charge overpotentials during the cycle.

The rate capabilities of PBI, PVDF, and PBI/PVDF composite binder cathodes were also evaluated at various discharge C rates from 0.1 C to 3.0 C and then back to 0.1 C. At 0.1 C,

both the PBI and PVDF cathodes showed similar specific discharge capacities of about 1050 mAh g^{-1} S, however, the specific discharge capacity of the PVDF cathode decreased dramatically as the test C-rate increased, and finally, a specific discharge capacity of only about 320 mAh g^{-1} S was obtained at 1.0 C discharge. In contrast, the PBI cathode retained a specific discharge capacity of about 600 mAh g^{-1} S at 1.0 C discharge, indicating that the PBI cathode could provide an electrode structure more suitable for high C-rates than the PVDF cathode. Furthermore, the PBI/PVDF composite binder cathode exhibited the best rate capability with a highly reversible discharge capacity of about 800 and 350 mAh g^{-1} S at C-rates of 1.0 and 3.0 C, respectively, and the specific discharge capacity recovered quickly to 1066 mAh g^{-1} S, when the C-rate was decreased back to 0.1 C.

To understand the longevity of Li–S cells configured with the different binders, cycling performance at 1.0 C over 150 cycles was evaluated for PBI, PVDF, and PBI/PVDF derived cathodes (Figure 2f). Compared to the PVDF cathode, the PBI cathode exhibited a reversible discharge capacity approximately 1.5−2 times higher after 150 cycles with a Coulombic efficiency above 99.4%. The Coulombic efficiency of the PVDF cathode was unstable, possibly due to incomplete Li_2S formation, accounting for the lack of a second discharge plateau shown in Figure 2d. On the other hand, the PBI/PVDF composite binder cathode exhibited excellent cycling performance at 1.0 C discharge with an initial discharge capacity around 700 mAh g^{-1} S. A specific discharge capacity of 600 mAh g^{-1} S was obtained after 150 cycles, which corresponds to a capacity retention of 86%. During 150 cycles, the Coulombic efficiency of the PBI/PVDF composite binder cathode was above 99.8%, reflecting the superior reversibility of the electrochemical reaction between sulfur and lithium during cycling with this binder blend.

Collectively, these initial experiments point to significant gains in high-rate performance when PBI is used as a binder in place of PVDF, and even greater gains when the PBI/PVDF blend is used. While there is a myriad of microscopic processes that dictate Li–S cell characteristics, the presence of these new PBI binders with turn-on activation for charge transfer and charge transport only amplifies that complexity as does the role played by PBI/PVDF interfaces. Thus, we were interested in applying additional electroanalytical techniques to our cathodes that might more directly relate the specific influence of the adaptive charge-transporting PBI networks on the observed cell performance.

To that end, we applied a galvanostatic intermittent titration technique (GITT) to study the evolution of ion-transport behaviors within the cathodes upon cycling. PBI, PVDF, and PBI/PVDF composite binder cathodes were cycled at 0.1 C with 45-min-long galvanostatic pulses, interrupted by 1 h of equilibration time between pulses (Figure 3a-c). Overpotentials at each point, determined by the potential difference between the end of the current step and the end of the equilibration step, are plotted as ΔE *vs*. state of charge (SOC) (Figure 3d). From these data, it was readily apparent that the open circuit potentials measured after the equilibration times were equivalent for all three cathodes; however, the hystereses of the cathodes were significantly different. In principle, the sudden potential change at short times is mainly due to an iR drop generated by the ohmic resistance of the cell,[49] and the PVDF cathode showed the highest overpotential at nearly all states of charge compared to the other two cathodes containing supramolecular PBI binder (Figure 3d). Notably, the PBI/PVDF blended binder cathode showed the lowest overpotential among all cathodes. At SOCs between 20−0% and 80−100% during discharge and charge processes, respectively, all three cathodes showed dramatic increases in the overpotential. In those regions, dissolved lithium polysulfides are re-deposited onto the embedded current collector surface, essentially forming insoluble Li_2S or sulfur films during discharge or charge, respectively. This deposition increases the internal resistance of the cell by impeding both electron and lithium ion conduction due to their insulating nature.[50] Although PBI and PVDF cathodes each show similar overpotentials during the initial discharge, there is a pronounced drop in charging overpotentials for the PBI cathode once it has been electrochemically activated, indicating a redox-mediating effect or, alternatively, a change in the local solvation of the PBI network upon reduction and lithiation.

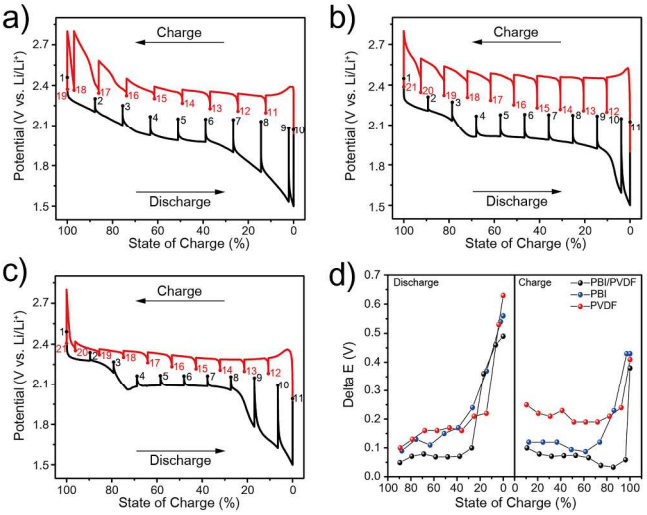

Figure 3. Voltage profiles of (a) PBI, (b) PVDF and (c) PBI/PVDF composite binder cathodes at 0.1C. Cathodes were discharged or charged in stages for 45 min, followed by 1 h of equilibration time. (0 % SOC is relative to the specific discharge capacity of the cathode at the end of discharge). Points are numbered in conjunction with data discussed in Figure 4. (d) Plot of polarization overpotential measured between the end of the current step and the end of the relaxations step.

Further insight into the emergent *in operando* behavior unique to cathodes prepared with PBI binders was gleaned from EIS measured at the end of every equilibration step throughout the GITT analysis (Figure 4). Nyquist plots of the PVDF cathode showed relatively large, depressed semicircles that increased in diameter as the SOC approached 0% and returned to near the original diameter upon charging to 100% SOC (Figure 4a-b), likely due to deposition and then dissolution of insulating Li_2S. A much more complex evolution of impedance spectra was observed in the case of PBI, where a depressed semicircle at high frequencies and a long sloping line at low frequencies was initially observed at 100% SOC (Figure 4c-d). Upon discharge, a second semicircle in the middle frequency region began to emerge (points 2−6) and by 27% SOC (point 7) the middle frequency semicircle began to

dominate the spectra with a sloping tail growing in the region between 40−80 mHz (points 7−9). Growth of a middle frequency semicircle has been previously attributed to the formation of a resistive Li_2S (or Li_2S_2) film on the sulfur cathode, which impedes diffusion of counterions and polysulfides to the current collector.[51,52] At the end of discharge (point 10) the semicircle in the middle frequency region and sloping line at low frequency are completely merged. This increase in impedance at 0% SOC may be due to mass-transport issues arising from the lower wettability of this cathode coupled with Li_2S deposits blocking ion transport near the current collector. Immediately upon charging, the large semicircle in the middle and low frequency regions disappeared and the impedance of the cell decreased dramatically. On the other hand, the PVDF/PBI composite binder cathode exhibited unique electrochemical behavior (Figure 4e-f), where the impedance decreased as the SOC approached 0% during discharge and the size of the semicircles remained small and nearly constant during the charge process, suggesting a unique activation had occurred *in operando*. Compared to the fully discharged PBI cathode, the PBI/PVDF composite binder cathode did not show any electrochemical behavior in the low frequency region that is associated with mass-transfer limitations. Instead, the EIS semicircles of the PBI/PVDF cathode were much smaller than those of the other two cathodes throughout the GITT, which is a sign of lower cell impedance overall and is in agreement with the enhanced rate capability during normal cell operation. Furthermore, this lowest-impedance state appears to be sustainable at different SOCs.

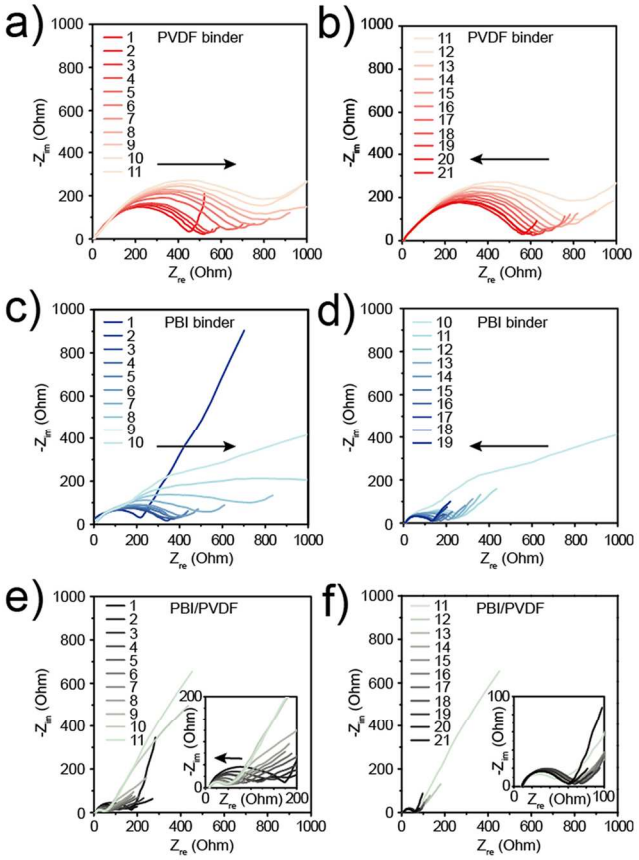

Figure 4. Nyquist plots of the PVDF cathode during (a) discharge (b) charge, PBI cathode during (c) discharge (d) charge, and PBI/PVDF composite binder cathode during (e) discharge (f) charge in the frequency range of 10 mHz to 1 MHz. Numbered spectra correspond to the points labeled in Figure 3a-c.

Our findings suggest a re-examination may be in order for the ideal binder paradigm for composite electrodes. Whereas passive binders impart many useful functions as noted, redox-active binders offer a powerful new means to adapt the electrode's transport behaviors *in operando* and on demand. Against conventional wisdom, we show that it is not necessary to configure the binder as a covalent high-polymer. Indeed, supramolecular approaches are also suitable; in fact, these may be preferred for electrode materials undergoing significant volume changes associated with conversion or alloying reactions, as is the case with sulfur and silicon electrodes. With this in mind, the networked architecture of the binder in the solid state and its relationship to the electrode's active materials and embedded current collector become key to understanding cell performance—with high interface density contributing favorably to high rate-performance as observed here with the PBI/PVDF-derived sulfur cathodes. We also suggest that we are only beginning to reveal the synergies between binder components, particularly with respect to their interactions with each other and with ions in the electrolyte. For example, we hypothesize that the evolved, low, and sustained cell impedance that we observe only in the case of electrochemically-activated PBI/PVDF blends may arise from improved charge-separation of both Li^+ (which coordinates to reduced Li_2-PBI) and $TFSI^-$ (which coordinates to PVDF), which would improve their mobility within the composite and thus enable the high-rate performance. These foundational concepts in adaptive transport behaviors begin to map forward an exciting path in materials discovery at the interface of organic, polymer, supramolecular, and electrochemistry.

ASSOCIATED CONTENT

Supporting Information

Materials, methods, active material preparation and characterization, cathode preparation and characterization, Li–S cell assembly and testing, and Supporting Figures S1–S9. The Supporting Information is available free of charge on the ACS Publications website.

AUTHOR INFORMATION

Corresponding Authors

* ejcairns@lbl.gov and bahelms@lbl.gov

Author Contributions

The manuscript was written through contributions of all authors.
‡These authors contributed equally.

ACKNOWLEDGMENT

Emory Chan is thanked for assistance with Raman spectroscopy. This work was partially supported by the Joint Center for Energy Storage Research, an Energy Innovation Hub funded by the U.S. Department of Energy, Office of Science, Office of Basic Energy Sciences. Portions of the work—including PBI synthesis, Raman spectroscopy, electron microscopy, and electrochemical testing of Li–S cells—were carried out as a user project at the Molecular Foundry, which is supported by the Office of Science, Office of

Basic Energy Sciences, of the U.S. Department of Energy under contract no. DE-AC02-05CH11231.

REFERENCES

[1] Bruce, P. G.; Freunberger, S. A.; Hardwick, L. J.; Tarascon, J.-M. Li–O_2 and Li–S batteries with high energy storage. *Nat. Mater.* **2012**, *11*, 19–29.

[2] Hwa, Y.; Cairns, E. J. *Li-Ion Batteries and Beyond: Future Design Challenges, Encyclopedia of Inorganic and Bioinorganic Chemistry*. John Wiley & Sons, **2015**.

[3] Ji, X. L.; Nazar, L. F. Advances in Li–S batteries. *J. Mater. Chem.* **2010**, *10*, 9821–9826.

[4] Yang, Y.; Zheng, G.; Cui, Y. Nanostructured sulfur cathodes. *Chem. Soc. Rev.* **2013**, *42*, 3018–3032.

[5] Manthiram, A.; Fu, Y.; Chung, S.-H.; Zu, C.; Su, Y.-S. Rechargeable Lithium–Sulfur Batteries. *Chem. Rev.* **2014**, *114*, 11751–11787.

[6] Li, W.; Yao, H.; Yan, K.; Zheng, G.; Liang, Z.; Chiang, Y.-M.; Cui, Y. The synergetic effect of lithium polysulfide and lithium nitrate to prevent lithium dendrite growth. *Nat. Commun.* **2015**, *6*, 7436.

[7] Chung, W. J.; Griebel, J. J.; Kim, E. T.; Yoon, H.; Simmonds, A. G.; Ji, H. J.; Dirlam, P. T.; Glass, R. S.; Wie, J. J.; Nguyen, N. A.; Guralnick, B. W.; Park, J.; Somogyi, A.; Theato, P.; Mackay, M. E.; Sung, Y.-E.; Char, K.; Pyun, J. The use of elemental sulfur as an alternative feedstock for polymeric materials. *Nat. Chem.* **2013**, *5*, 518–524.

[8] Simmonds, A. G.; Griebel, J. J.; Park, J.; Kim, K. R.; Chung, W. J.; Oleshko, V. P.; Kim, J.; Kim, E. T.; Glass, R. S.; Soles, C. L.; Sung, Y.-E.; Char, K.; Pyun, J. Inverse Vulcanization of Elemental Sulfur to Prepare Polymeric Electrode Materials for Li–S Batteries. *ACS Macro Lett.* **2014**, *3*, 229–232.

[9] Zheng, G.; Zhang, Q.; Cha, J. J.; Yang, Y.; Li, W.; Seh, Z. W.; Cui, Y. Amphiphilic Surface Modification of Hollow Carbon Nanofibers for Improved Cycle Life of Lithium Sulfur Batteries. *Nano Lett.* **2013**, *13*, 1265–1270.

[10] Ji, X.; Lee, K. T.; Nazar, L. F. A highly ordered nanostructured carbon–sulphur cathode for lithium–sulphur batteries. *Nat. Mater.* **2009**, *8*, 500–506.

[11] Zu, C.; Manthiram, A. Hydroxylated Graphene–Sulfur Nanocomposites for High-Rate Lithium–Sulfur Batteries. *Adv. Energy Mater.* **2013**, *3*, 1008–1012.

[12] Ji, L.; Rao, M.; Zheng, H.; Zhang, L.; Li, Y.; Duan, W.; Guo, J.; Cairns, E. J.; Zhang, Y. Graphene Oxide as a Sulfur Immobilizer in High Performance Lithium/Sulfur Cells. *J. Am. Chem. Soc.* **2011**, *133*, 18522–18525.

[13] Song, M.-K.; Zhang, Y.; Cairns, E. J. A Long-Life, High-Rate Lithium/Sulfur Cell: A Multifaceted Approach to Enhancing Cell Performance. *Nano Lett.* **2013**, *13*, 5891–5899.

[14] Hwa, Y.; Zhao, J.; Cairns, E. J. Lithium Sulfide (Li2S)/Graphene Oxide Nanospheres with Conformal Carbon Coating as a High-Rate, Long-Life Cathode for Li/S Cells. *Nano Lett.* **2015**, *15*, 3479–3486.

[15] Guo, J.; Yang, Z.; Yu, Y.; Abruña, H. D.; Archer, L. A. Lithium–Sulfur Battery Cathode Enabled by Lithium–Nitrile Interaction. *J. Am. Chem. Soc.* **2013**, *135*, 763–767.

[16] Song, J.; Gordin, M. L.; Xu, T.; Chen, S.; Yu, Z.; Sohn, H.; Lu, J.; Ren, Y.; Duan, Y.; Wang, D. Strong Lithium Polysulfide Chemisorption on Electroactive Sites of Nitrogen-Doped Carbon Composites For High-Performance Lithium–Sulfur Battery Cathodes. *Angew. Chem.* **2015**, *127*, 4399–4403.

[17] Tang, C.; Zhang, Q.; Zhao, M.-Q.; Huang, J.-Q.; Cheng, X.-B.; Tian, C.-L.; Peng, H.-J.; Wei, F. Nitrogen-Doped Aligned Carbon Nanotube/Graphene Sandwiches: Facile Catalytic Growth on Bifunctional Natural Catalysts and Their Applications as Scaffolds for High-Rate Lithium-Sulfur Batteries. *Adv. Mater.* **2014**, *26*, 6100–6105.

[18] Rao, M.; Song, X.; Cairns, E. J. Nano-carbon/sulfur composite cathode materials with carbon nanofiber as electrical conductor for advanced secondary lithium/sulfur cells. *J. Power Sources* **2012**, *205*, 474–478.

[19] Jozwiuk, A.; Sommer, H.; Janek, J.; Brezesinski, T. Fair performance comparison of different carbon blacks in lithium–sulfur batteries with practical mass loadings – Simple design competes with complex cathode architecture. *J. Power Sources* **2015**, *296*, 454–461.

[20] Pang, Q.; Liang, X.; Kwok, C. Y.; L. F. Nazar, L. F. Review—The Importance of Chemical Interactions between Sulfur Host Materials and Lithium Polysulfides for Advanced Lithium-Sulfur Batteries. *J. Electrochem. Soc.* **2015**, *162*, A2567–A2576.

[21] Chung, S.-H.; Manthiram, A. Nano-cellular carbon current collectors with stable cyclability for Li–S batteries. *J. Mater. Chem. A* **2013**, *1*, 9590–9596.

[22] Cheng, X.-B.; Peng, H.-J.; Huang, J.-Q.; Zhu, L.; Yang, S.-H.; Liu, Y.; Zhang, H.-W.; Zhu, W.; Wei, F.; Zhang, Q. Three-dimensional aluminum foam/carbon nanotube scaffolds as long- and short-range electron pathways with improved sulfur loading for high energy density lithium–sulfur batteries. *J. Power Sources* **2014**, *261*, 264–270.

[23] Zhou, G.; Li, L.; Ma, C.; Wang, S.; Shi, Y.; Koratkar, N.; Ren, W.; Li, F.; Cheng, H.-M. A graphene foam electrode with high sulfur loading for flexible and high energy Li-S batteries. *Nano Energy* **2015**, *11*, 356–365.

[24] Mikhaylik, Y. V.; Akridge, J. R. Polysulfide Shuttle Study in the Li/S Battery System. *J. Electrochem. Soc.* **2004**, *151*, A1969–A1976.

[25] Choi, N.-S.; Chen, Z.; Freunberger, S. A.; Ji, X.; Sun, Y.-K.; Amine, K.; Yushin, G.; Nazar, L. F.; Cho, J.; Bruce, P. G. Challenges facing lithium batteries and electrical double-layer capacitors. *Angew. Chem. Int. Ed.* **2012**, *51*, 9994–10024.

[26] Lacey, M. J.; Jeschull, F.; Edström, K.; Brandell, D. Porosity Blocking in Highly Porous Carbon Black by PVdF Binder and Its Implications for the Li–S System. *J. Phys. Chem. C* **2014**, *118*, 25890–25898.

[27] Huang, Y.; Sun, J.; Wang, W.; Wang, Y.; Yu, Z.; Zhang, H.; Wang, A.; Yuan, K. Lithium Sulfur Battery Oxidation/Reduction Mechanisms of Polysulfides in THF Solutions. *J. Electrochem. Soc.* **2008**, *155*, A764–A767.

[28] Seh, Z. W.; Zhang, Q.; Li, W.; Zhen, G.; Yao, H.; Cui, Y. Stable cycling of lithium sulfide cathodes through strong affinity with a bifunctional binder. *Chem. Sci.* **2013**, *4*, 3673–3677.

[29] Wang, Q.; Yan, N.; Wang, M.; Qu, C.; Yang, X.; Zhang, H.; Li, X.; Zhang, H. Layer-by-Layer Assembled C/S Cathode with Trace Binder for Li–S Battery Application. *ACS Appl. Mater. Interfaces* **2015**, *7*, 25002–25006.

[30] Bhattacharya, P.; Nandasiri, M. I.; Lv, D.; Schwarz, A. M.; Darsell, J. T.; Henderson, W. A.; Tomalia, D. A.; Liu, J.; Zhang, J.-G.; Xiao, J. A novel separator coated by carbon for achieving exceptional high performance lithium-sulfur batteries. *Nano Energy* **2016**, *19*, 176–184.

[31] Zeng, F.; Wang, W.; Wang, A.; Yuan, K.; Jin, Z.; Yang, Y.-S. Multidimensional Polycation β-Cyclodextrin Polymer as an Effective Aqueous Binder for High Sulfur Loading Cathode in Lithium–Sulfur Batteries. *ACS Appl. Mater. Interfaces* **2015**, *7*, 26257–26265.

[32] Lee, J. T.; Zhao, Y.; Thieme, S.; Kim, H.; Oschatz, M.; Borchardt, L.; Magasinski, A.; Cho, W.-I.; Kaskel, S.; Yushin, G. Sulfur-Infiltrated Micro- and Mesoporous Silicon Carbide-Derived Carbon Cathode for High-Performance Lithium Sulfur Batteries. *Adv. Mater.* **2013**, *25*, 4573–4579.

[33] Lacey, M. J.; Jeschull, F.; Edstrom, K.; Brandell, D. Functional, water-soluble binders for improved capacity and stability of lithium–sulfur batteries. *J. Power Sources* **2014**, *264*, 8–14.

[34] Rao, M.; Song, X.; Liao, H.; Cairns, E. J. Carbon nanofiber–sulfur composite cathode materials with different binders for secondary Li/S cells. *Electrochim. Acta* **2012**, *65*, 228–231.

[35] He, M.; Yuan, L.-X.; Zhang, W.-X.; Hu, X.-L.; Huang, Y.-H. Enhanced Cyclability for Sulfur Cathode Achieved by a Water-Soluble Binder. *J. Phys. Chem. C* **2011**, *155*, 15703–15709.

[36] Ai, G.; Dai, Y.; Ye, Y.; Mao, W.; Wang, Z.; Zhao, H.; Chen, Y.; Zhu, J.; Fu, Y.; Battaglia, V.; Guo, J.; Srinivasan, V.; Liu, G. Investigation of surface effects through the application of the functional binders in lithium sulfur batteries. *Nano Energy* **2015**, *16*, 28–37.

[37] Li, X.; Cao, Y.; Qi, W.; Saraf, L. V.; Xiao, J.; Nie, Z.; Mietek, J.; Zhang, J.-G.; Schwenzer, B.; Liu, J. Optimization of mesoporous carbon structures for lithium–sulfur battery applications. *J. Mater. Chem.* **2011**, *21*, 16603–16610.

[38] Li, W.; Zhang, Q.; Zheng, G.; Seh, Z. W.; Yao, H.; Cui, Y. Understanding the Role of Different Conductive Polymers in Improving the Nanostructured Sulfur Cathode Performance. *Nano Lett.* **2013**, *13*, 5534–5540.

[39] Li, X.-Q.; Stepanenko, V.; Chen, Z.; Prins, P.; Siebbeles, L. D. A.; Würthner, F. Functional organogels from highly efficient organogelator based on perylene bisimide semiconductor. *Chem. Commun.* **2006**, 3871–3873.

[40] Frischmann, P. D.; Gerber, L. C. H.; Doris, S. E.; Tsai, E. Y.; Fan, F. Y.; Qu, X.; Jain, A.; Persson, K. A.; Chiang, Y.-M.; Helms, B. A. Supramolecular Perylene Bisimide-Polysulfide Gel Networks as Nanostructured Redox Mediators in Dissolved Polysulfide Lithium–Sulfur Batteries. *Chem. Mater.* **2015**, *27*, 6765–6770.

[41] Gerber, L. C. H.; Frischmann, P. D.; Fan, F. Y.; Doris, S. E.; Qu, X.; Scheuermann, A. M.; Persson, K.; Chiang, Y.-M.; Helms, B. A. Three-Dimensional Growth of Li2S in Lithium–Sulfur Batteries Promoted by a Redox Mediator. *Nano Lett.* **2016**, *16*, 549–554.

[42] Meini, S.; Elazari, R.; Rosenman, A.; Garsuch, A.; Aurbach, D. The Use of Redox Mediators for Enhancing Utilization of Li2S Cathodes for Advanced Li–S Battery Systems. *J. Phys. Chem. Lett.* **2014**, *5*, 915–918.

[43] Li, J.; Yang, L.; Yang, S.; Lee, J. Y. The Application of Redox Targeting Principles to the Design of Rechargeable Li–S Flow Batteries. *Adv. Energy Mater.* **2016**, *5*, 1501808.

[44] Würthner, F. Perylene bisimide dyes as versatile building blocks for functional supramolecular architectures. *Chem. Commun.* **2004**, 1564–1579.

[45] Zhan, X.; Facchetti, A.; Barlow, S.; Marks, T. J.; Ratner, M. A.; Wasielewski, M. R.; Marder, S. R. Rylene and Related Diimides for Organic Electronics. *Adv. Mater.* **2011**, *23*, 268–284.

[46] Rey, I.; Johansson, P.; Lindgren, J.; Lassègues, J. C.; Grondin, J.; Servant, L. Spectroscopic and Theoretical Study of $(CF_3SO_2)_2N^-$ ($TFSI^-$) and $(CF_3SO_2)_2NH$ (HTFSI). *J. Phys. Chem. A* **1998**, *102*, 3249−3258.

[47] Herstedt, M.; Smirnov, M.; Johansson, P.; Chami, M.; Grondin, J.; Servant, L.; Lassègues, J. C. Spectroscopic characterization of the conformational states of the bis(trifluoromethanesulfonyl)imide anion ($TFSI^-$). *J. Raman Spectrosc.* **2005**, *36*, 762−770.

[48] Seo, D. M.; Boyle, P. D.; Sommer, R. D.; Daubert, J. S.; Borodin, O.; Henderson, W. A. Solvate Structures and Spectroscopic Characterization of LiTFSI Electrolytes. *J. Phys. Chem. B* **2014**, *118*, 13601−13608.

[49] Weppner, W.; Huggins, R. A. Determination of the Kinetic Parameters of Mixed-Conducting Electrodes and Application to the System Li_3Sb. *J. Electrochem. Soc.* **1977**, *124*, 1569–1578.

[50] Yang, Y.; Zheng, G.; Misra, S.; Nelson, J.; Toney, M. F.; Cui, Y. High-Capacity Micrometer-Sized Li_2S Particles as Cathode Materials for Advanced Rechargeable Lithium-Ion Batteries. *J. Am. Chem. Soc.* **2012**, *134*, 15387–15394.

[51] Yuan, L.; Qiu, X.; Chen, L.; Zhu, W. New insight into the discharge process of sulfur cathode by electrochemical impedance spectroscopy. *J. Power Sources*, **2009**, *189*, 127–132.

[52] Canas, N. A.; Hirose, K.; Pascucci, B.; Wagner, N.; Friedrich, K. A.; Hiesgen, R. Investigations of lithium–sulfur batteries using electrochemical impedance spectroscopy. *Electrochim. Acta*, **2013**, *97*, 42–51.

Table of Contents artwork

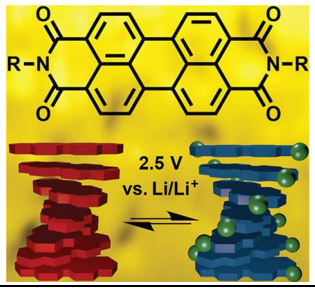

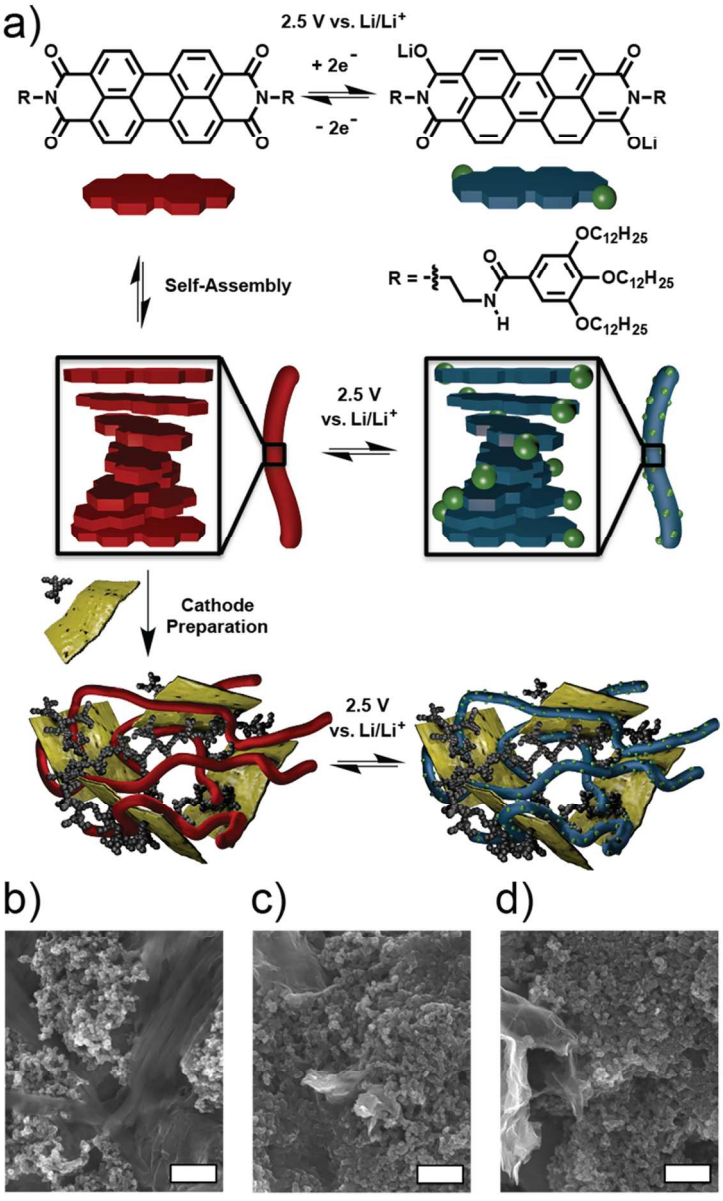

83x138mm (300 x 300 DPI)

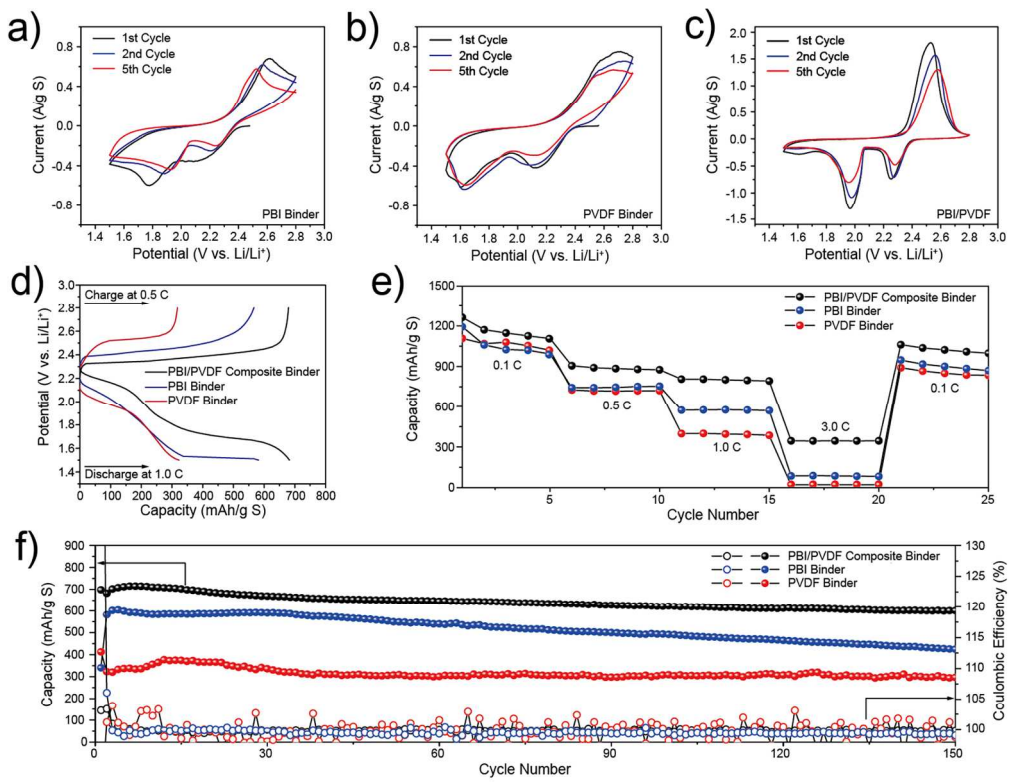

177x142mm (300 x 300 DPI)

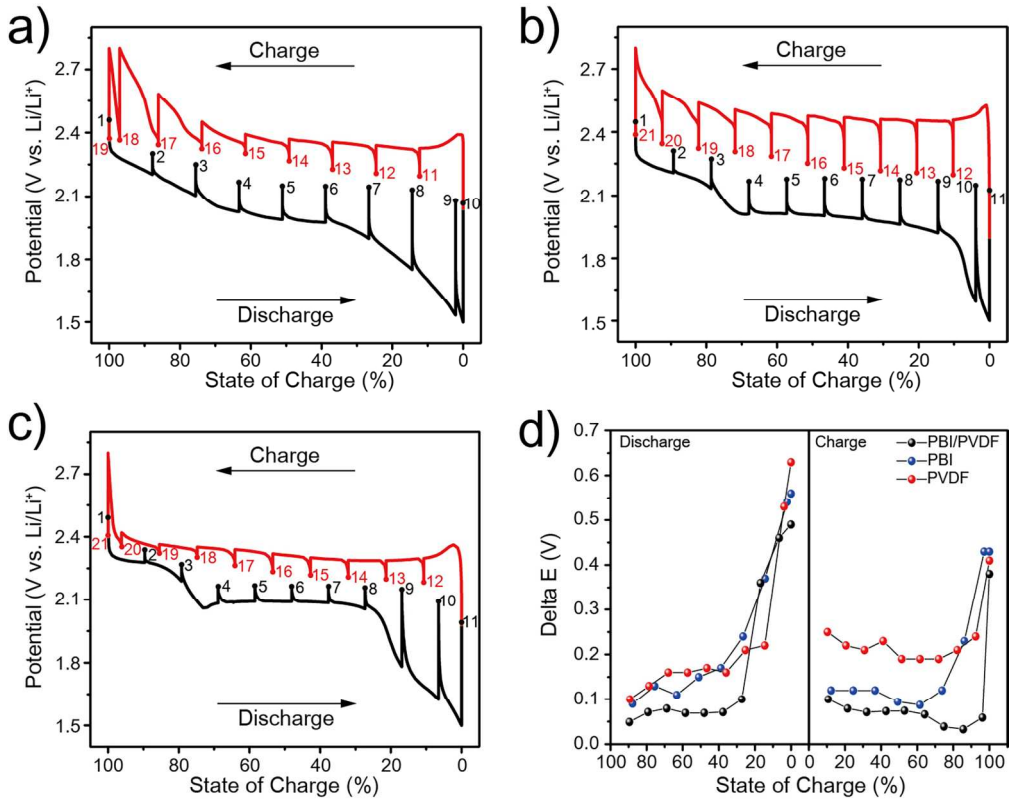

177x142mm (300 x 300 DPI)

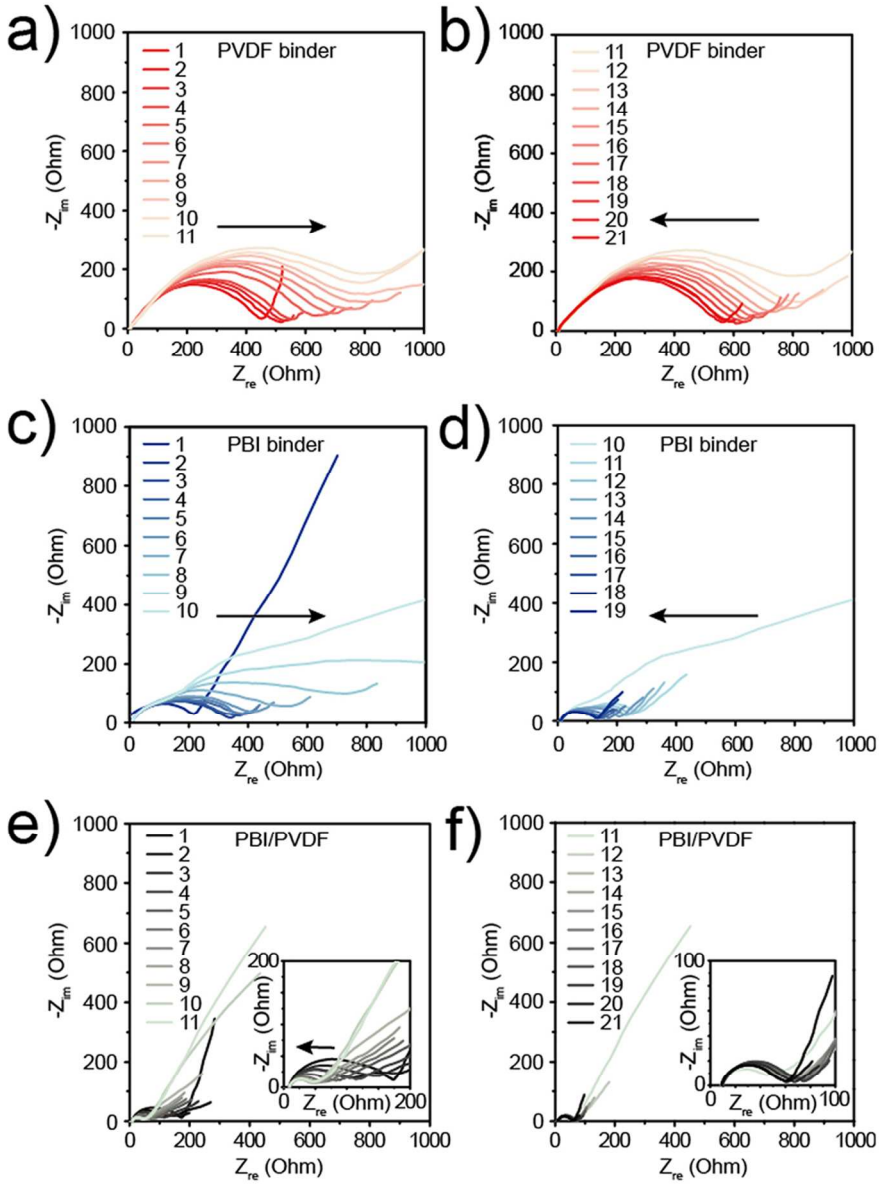

83x114mm (300 x 300 DPI)

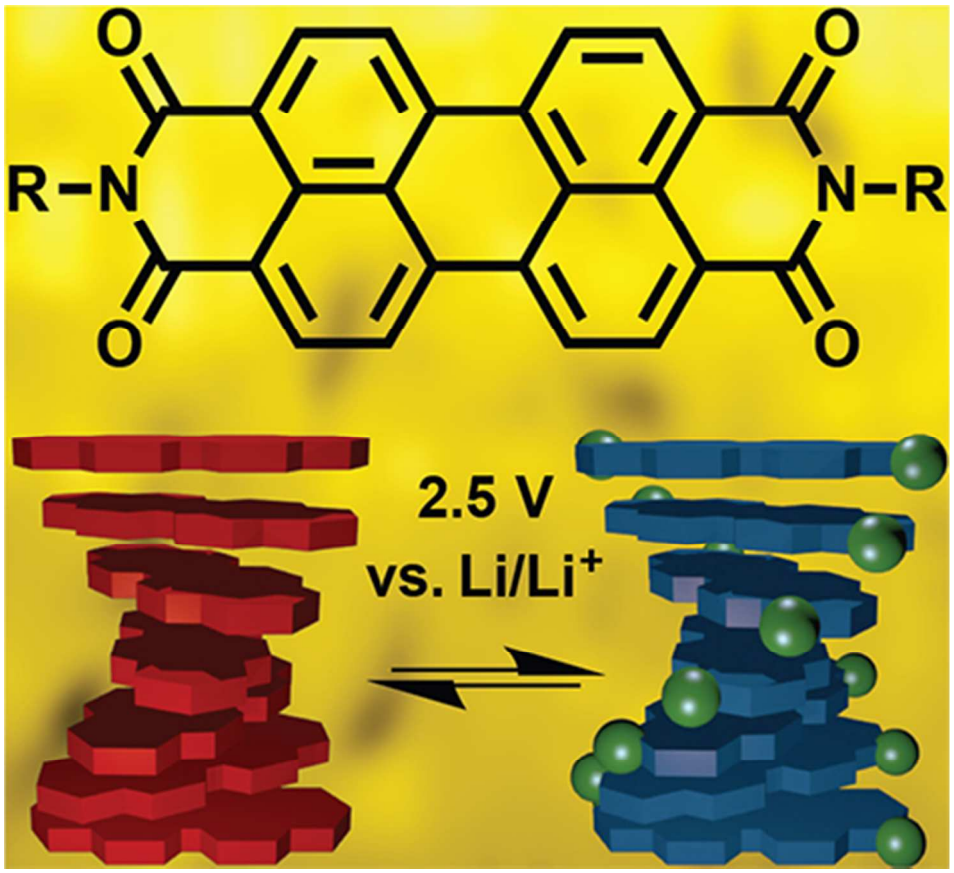

39x36mm (300 x 300 DPI)